New Journal and we have not received input yet 28 (2021) 100258

Contents lists available at ScienceDirect

FlatChem

journal homepage: www.sciencedirect.com/journal/flatchem

Spongy-like N, S-codoped ultrathin layered carbon assembly for realizing high performance sodium-ion batteries

Lin Sun [a,b,*], Xinyu Song [a], Yanxiu Liu [a], Jie Xie [a], Jun Wu [a], Feng Cheng [a,*], Xiaoli Zhang [c], Zuoxiu Tie [b,d], Zhong Jin [b,d,*]

[a] School of Chemistry and Chemical Engineering, Yancheng Institute of Technology, Yancheng 224051, China
[b] MOE Key Laboratory of Mesoscopic Chemistry, MOE Key Laboratory of High Performance Polymer Materials and Technology, Jiangsu Key Laboratory of Advanced Organic Materials, School of Chemistry and Chemical Engineering, Nanjing University, Nanjing 210023, China
[c] School of Materials Science and Engineering, Zhengzhou University, Zhengzhou 450001, China
[d] Shenzhen Research Institute of Nanjing University, Shenzhen 518063, China

ARTICLE INFO

Keywords:
Sodium ion battery, carbon material
N, S-codoping
Anode
Two-dimensional structure

ABSTRACT

Sodium-ion batteries (SIBs) are being increasingly studied due to their cost-effectiveness, high energy density and abundant resources. However, because of scanty interlayer spacing, commercial graphite-based materials that are currently used in lithium-ion batteries (LIBs) are not compatible for SIB anodes. Herein, we design a very convenient template strategy to synthesize spongy-like N, S-codoped ultrathin layered carbon assembly (NSLCA) with high N (9.5%) and S (1.7%) contents as an advanced anode material for SIBs. A petroleum-derived sulfur-containing pitch is chosen as the carbon skeleton, thus simplifying the preparation steps and reducing the costs. With the help of nanoporous MgO templates, the ultrathin layered carbon assembly can be facilely prepared. In addition, benefitting from the synergistic effects of codoped abundant N and S, as well as its unique assembly structures, the NSLCA anode exhibits outstanding sodium storage performance, with an especially superior rate performance (256 mA h g^{-1} at a current density of 3 A g^{-1}) and a long lifespan (charge–discharge for as many as 2000 cycles with no capacity decay). This study provides a feasible and convenient strategy for the convenient and batch production of a spongy-like N, S-codoped carboneous material towards the construction of high-performance and cost-effectiveness SIBs.

1. Introduction

The ongoing shortage of the world's nonrenewable resources is urgently in need of energy harvesting with high energy density in large-scale to make use of renewable sources such as wind and solar power [1]. In the past two decades, we have witnessed the growth and development of lithium-ion batteries (LIBs), which are increasingly important for mobile applications as well as for grid-scale stationary storage [2,3]. However, the high cost and finite supply of lithium severely hinder commercial LIBs from meeting the above requirements [4]. As one of most promising candidates for next-generation energy storage systems, sodium-ion batteries (SIBs) have been increasingly studied based on the natural abundance and lower prices of metallic sodium [5–7]. Nevertheless, for a variety of anodic materials, the ion transmission kinetics and structural integrity during the charge/discharge process are seriously influenced by the high redox potential of Na^+/Na (−2.71 V, vs. Li^+/Li, −3.04 V) and sluggish Na^+ migration (the radius of Na^+ is significantly greater than that of Li^+) [8]. To address the aforementioned issues, great research efforts have been devoted to fabricating anode materials suitable for both LIBs and SIBs. For instance, previous works have revealed that Na^+ is preferentially adsorbed on the surface of a carbon host and inserted between lattice spaces and carbon layers, which is defined as an adsorption-intercalation mechanism [1,9,10]. Therefore, it is imperative to develop anodic materials with large interlayers to embrace the unhindered intercalation and deintercalation of sodium ions, thereby improving the sodium storage capacity and prolonging the lifespan of the battery.

A large number of noncarbonaceous materials with different sodium

* Corresponding authors at: School of Chemistry and Chemical Engineering, Yancheng Institute of Technology, Yancheng 224051, China (L. Sun). MOE Key Laboratory of Mesoscopic Chemistry, MOE Key Laboratory of High Performance Polymer Materials and Technology, Jiangsu Key Laboratory of Advanced Organic Materials, School of Chemistry and Chemical Engineering, Nanjing University, Nanjing 210023, China (Z. Jin).
E-mail addresses: sunlin@nju.edu.cn (L. Sun), chf@nju.edu.cn (F. Cheng), zhongjin@nju.edu.cn (Z. Jin).

https://doi.org/10.1016/j.flatc.2021.100258
Received 21 May 2021; Received in revised form 28 May 2021; Accepted 3 June 2021
Available online 8 June 2021

storage mechanisms have been developed as anodes for SIBs, including metal oxides/sulfides (e.g., TiO_2 [11,12], SnS_2 [13,14], MoS_2 [15,16]) and metals/alloys (e.g., Sn [17,18], $NiSe_2$ [19]). In general, these materials still suffer severe volume changes when Na^+ is inserted, leading to decreased cycling stability. Instead, rational design and facile synthesis of non-noble materials for SIBs are highly demanded, carbonaceous materials featuring an inexpensive and abundant supply have been extensively studied as anodes for SIBs. However, some disadvantages such as ultralow theoretical specific capacity, and unsatisfied rate capability impede the actual applications of perfectly structured graphite in high-energy–density SIBs. Alternatively, other carbon substances, including porous carbon [20], heteroatom-doped carbon [21] and carbons with various structures [22], have been employed and studied as anode materials to boost the energy and power densities of rechargeable secondary batteries. As mentioned above, one of the most effective routes to increase the sodium storage capacity of carbonaceous electrodes is the elaborate combination of the structural design and interlayer expansion of carbon hosts to accommodate more intercalated sodium ions. Generally, elements with a larger atomic radius than carbon, such as sulfur (S) and phosphorus (P), can enlarge carbon interlayers. For example, Ye et al. reported a multistep method to obtain porous hard carbon nanospheres codoped with sulfur and nitrogen. When serving as anodes for SIBs, these porous carbon electrodes exhibited high performance accompanied with a long lifespan and superior rate capability [23]. Wang et al. proposed a novel dense and P, -N codoped carbon derived from bacterial cellulose (BC) with crosslinked with hexachlorocyclotriphosphazene (HCCP), simultaneously combining a high volumetric and gravimetric capacity [24]. However, a better carbon-based material for sodium storage that simultaneously integrates facile preparation, high capacity, superior rate performance and prolonged lifespan has rarely been reported thus far. Therefore, it is still highly desirable to develop carbon-based anodes for high-performance SIBs.

To obtain carbonaceous materials with excellent comprehensive performance, while decreasing the synthesis cost, the selected precursor for carbonization is essential. Herein, we present a facile templating method to obtain a spongy-like N, S-codoped ultrathin layered carbon assembly (NSLCA) on a batch scale. Oil-derived pitch is selected as the carbon skeleton due to its abundance in the petrochemical industry and the intrinsic sulfur that it contains. In addition, the layered porous MgO layer serves as a hard template, and melamine particles provide the nitrogen source. When serving as an anode for SIBs, the novel NSLCA electrode delivers a reversible capacity as high as 500 mA h g^{-1} at a current density of 0.1 A g^{-1}, and even when the current density is increased to 2 A g^{-1}, the reversible capacity remains 260 mA h g^{-1} after deep cycling for 2000 cycles. In combination with theoretical calculations and reaction kinetic analysis, including ex situ X-ray diffraction (XRD), transmission electron microscopy (TEM), X-ray photoelectron spectroscopy (XPS) and cyclic voltammetry (CV), S doping can significantly spread apart the interlayers of carbon, while the pyrrolic and pyridinic N are the main contributors to the improved capacity. Concurrently, the unique spongy-like continuous network architectures enable the rapid electron mobility and the reduction of interfacial resistance. It is believed that this work will provide new insights into the facile preparation of heteroatom-doped hierarchical carbons that will be studied further in the areas of materials science and rechargeable batteries.

2. Experimental

2.1. Synthesis of porous MgO template

Typically, purchased MgO powder was dispersed in deionized water with ultrosonic agitation. The formed mixture was boiled for 24 h in a reflux apparatus. The obtained material was calcined at 500℃ for 30 min after filtration and drying to afford porous MgO.

2.2. Synthesis of spongy-like N, S-codoped ultrathin layered carbon assembly (NSLCA)

In a typical synthesis process, pitch powder, porous MgO template and melamine were uniformly mixed in ethanol in the proportion of 1:1:1 in weight. After continuous stirring and drying in oven at 80 °C, a grey powder mixture was obtained. The powder was then crushed and calcined in a quartz tube under 700 °C for 30 min with argon protection. The obtained black powder was treated by hydrochloric acid washing. After washing and drying, the spongy-like N, S-codoped ultrathin layered carbon assembly (NSLCA) was finnally obtained. For comparison, single S-doped carbon (designated as SLCA) was prepared by treating the mixture of MgO and pitch (1:1 in weight) as above.

2.3. Characterizations

Powder X-ray diffraction (PXRD) was performed on a X'Pert3Powder instrument (PANalytical, Netherland) using a Cu Kα radiation at room temperature. Scanning electron microscopy (SEM) was conducted on a Nova NanoSEM 450 field-emission scanning electron microscope at acceleration voltages of 15 kV. Transmission electron microscopy (TEM) and energy dispersive X-ray spectroscopy (EDS) were carried out using a JEM-1400-plus instrument (Japan). Atomic force microscopy (AFM) was conducted using a SPI3800/SPA400 instrument (Seiko Inc., Japan). Raman spectroscopy (InVia-Reflex, Renishaw) was performed with a laser source of 633 nm wavelength. X-ray photoelectron spectroscopy (XPS) data were collected with a ESCALAB 250Xi (Thermo Fisher Scientific). Nitrogen adsorption/desorption test were carried out at 77 K using Micrometrics ASAP 2020 analyzer after vacuum degassing of the samples at 120 ℃ for 8 h. Fourier transform infrared spectroscopy (FTIR) spetra was obtaiend using a NEXUS-670 apparatus.

2.4. Electrochemical measurements

Coin cells (CR2025) were employed to evaluate the electrochemical performance of the obtained NSLCA product. The assemblly process was performed in an Ar gas-filled glove box with both H_2O and O_2 lower than 0.1 ppm. The weight ratio of active material, conductive graphite, and polyvinylidene fluoride (PVDF) binder was fixed at 8:1:1. The formed slurry was stirred in deionized water and blade-coated on a Cu foil with coarse surface. After drying at 90 ℃ in vacuum for 10 h, the coated Cu foil was cut into disks with 12 mm in diameter. The electrolyte consisted of a solution of 1.0 M $NaClO_4$ in a mixture of ethylene carbonate (EC)/dimethyl carbonate (DMC) with volume ratio of 1:1; in addition, 5 wt% of fluoroethylene carbonate (FEC) was added in the electrolyte to improve the performance. The counter electrode was pure Na slices. The charge–discharge tests were performed on a Neware battery testing system (Shenzhen, China) at the constant current mode in the voltage range of 0.01–3.0 V. The specific capacities were calculated based on the total weight of active materials. The loading weight of active material was fixed at ~ 1.0 mg cm^{-2}.

2.5. Theoretical calculations

Theoretical calculations based on DFT were performed in this work by using the Vienna ab initio simulation package (VASP). The projector-augmented-wave (PAW) [25] potentials were adopted while the generalized gradient approximations (GGA) of Perdew–Burke–Ernzerhof (PBE) [26] pseudopotentials were applied for the exchange–correlation functional. The binding energy (E_b) was calculated using the formular of $E_b = E_t - E_{sr} - E_{Na}$, where E_t is the total energy of the adsorbed system, $E_{sr}$is the total energy of the surface, and $E_{Na}$is the total energy of the isolated Na atom. Herein, more negtive values demostrate the possibility of adsorbate–surface interactions due to the energy advantage.

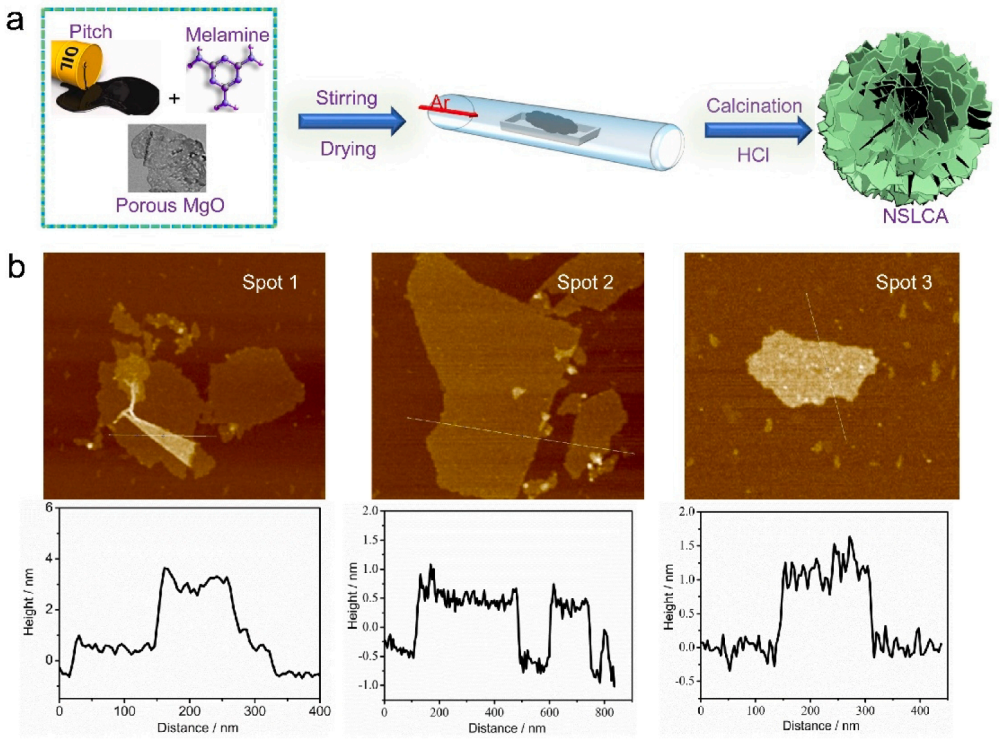

Fig. 1. (a) Schematic illustration showing the preparation of NSLCA and the (b) AFM measurements of the NSLCA.

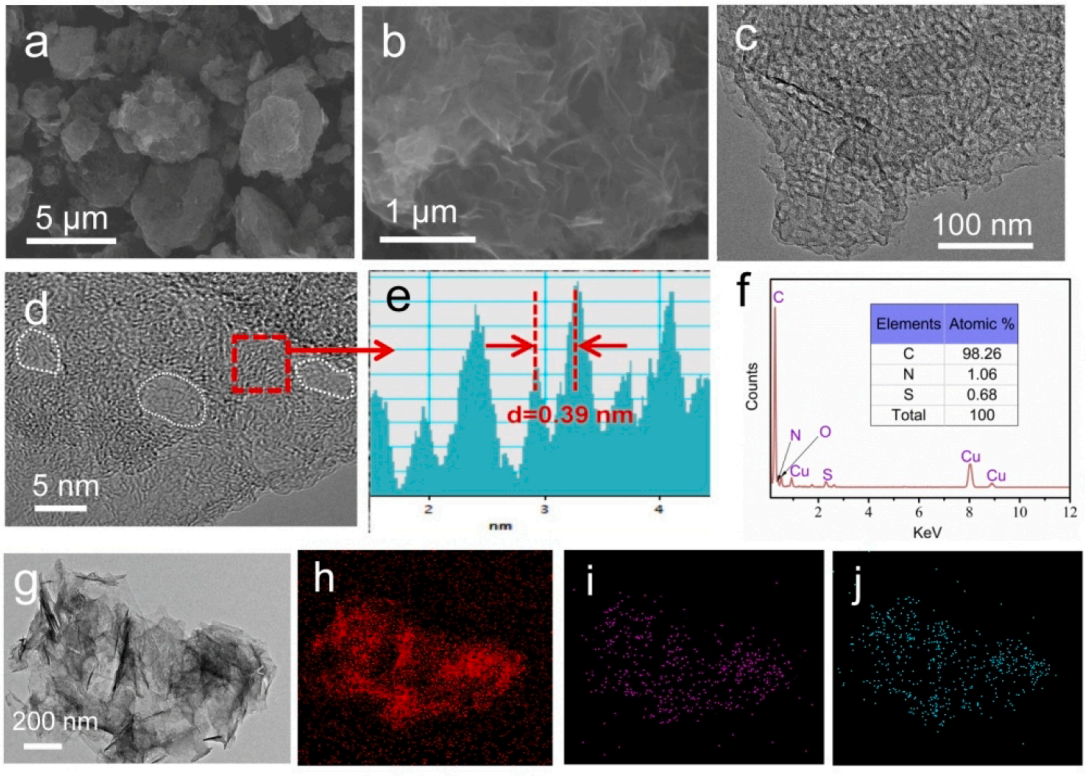

Fig. 2. (a, b) SEM images, (c, d) TEM and HRTEM images, (e) Corresponding intensity profile for the lattice fringes in the marked region, and (f) EDS spectrum of NSLCA; (g-j) TEM image and corresponding elemental mapping of NSLCA, (h), (i), and (j) S are assigned to element C, N and S, respectively.

3. Results and discussion

The process for preparing NSLCA is schematically illustrated in Fig. 1a. Dual-component doped layered carbonaceous materials were synthesized via a facile method using layered porous MgO and melamine as templates and nitrogen sources, respectively, the details are in the

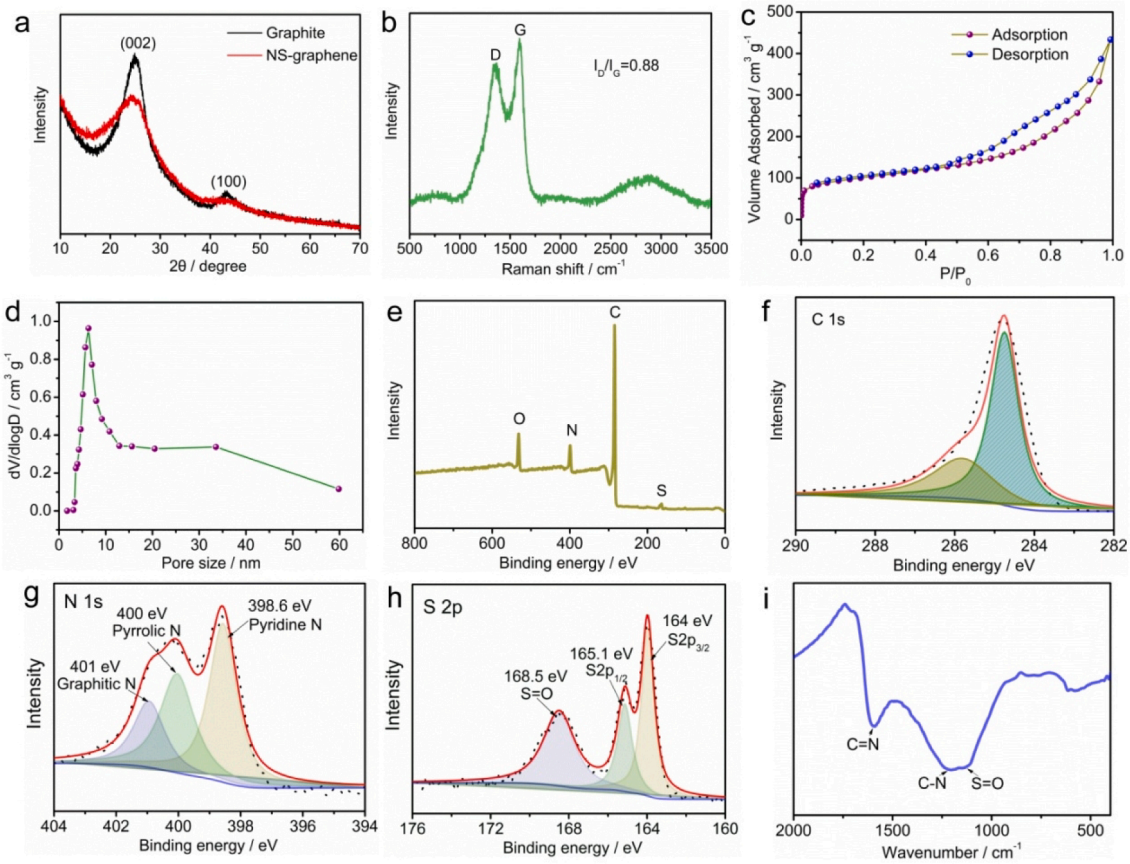

Fig. 3. (a) XRD patterns of the graphite and NSLCA. (b) Raman spectra, (c) N_2 isothermal adsorption and desorption, and (d) pore size distribution of the NSLCA. (e) Survey, (f) C 1s, (g) N 1s, and (h) S 2p XPS spectra of the NSLCA. (i) FTIR spectrum of the NSLCA.

Experimental section. As a comparison, bare sulfur-doped layered carbon assembly (SLCA) was obtained according to the same preparation procedure without the addition of melamine. Herein, as shown in Fig. S1a, the MgO powders used in this work exhibit porous sheet-like structures, and regular lattice fringes with a *d*-spacing of 0.152 nm are further confirmed with high-resolution transmission electron microscopy (HRTEM). As shown in Fig. S1b, the insert Fourier transform diffraction explicitly demonstrates the exposure of the (220) lattice plane of MgO [27].

The morphology, chemical components, and elemental distributions of the prepared NSLCA were characterized by scanning electron microscopy (SEM), transmission electron microscopy (TEM), atomic force microscopy (AFM) and energy dispersive spectroscopy (EDS), as shown in Fig. 1b and Fig. 2. The thickness of the ultrathin structures was investigated by AFM measurements, which are presented in Fig. 1b. The average thickness of the obtained NSLCA are calculated as 1–3 nm, implying that a large lateral-to-thickness ratio is very beneficial for electron mobility. The SEM images in Fig. 2a and b demonstrate that the bulk agglomerated structures are assembled by wrinkled nanosheets. Furthermore, as presented in Fig. 2c and d, TEM and HRTEM images clearly confirm the wrinkled nanosheet and the presence of mesoporous structures that possibly stem from the porous Mg template, the mean size of the mesopores is ~5–10 nm. Moreover, it is found from Fig. 2e that the NSLCA sample exhibits a well-defined ultrathin layered structure with an interlayer spacing of 0.39 nm, corresponding to the enlarged (002) planes of graphite. Furthermore, The EDS analysis (Fig. 2f) of NSLCA displays the content of doped N and S is 1.06 and 0.68 (atomic %), and the presence and homogeneous distributions of N and S elements are verified by the corresponding elemental mapping (Fig. 2g, h, i and j).

Powder X-ray diffraction (XRD) analysis was employed to investigate the crystalline phase of the prepared samples. As illustrated in Fig. 3a, the XRD patterns of both the NSLCA and graphite show a sharp peak at approximately 25° and another weak peak at approximately 44°, which can be assigned to the typical (002) and (100) planes of carbon, respectively. Moreover, compared with graphite, it should be noted that the peak location of the (002) plane for NSLCA is slightly lower, signifying enlarged d-spacing [28], which is consistent with the TEM results. At the same time, the broadened peak width of the NSLCA also confirms the very thin structures. The Raman spectrum of the NSLCA is presented in Fig. 3b, showing the D band at 1340 cm^{-1} (defects) and the G band at 1580 cm^{-1} (crystalline graphite) [29]. The peak intensity ratio of the D to G band (I_D/I_G) is 3.2, implying the presence of abundant defects in the NSLCA sample. Moreover, the N_2 sorption isotherms and pore size distributions of NSLCA are presented in Fig. 3c and d. Fig. 3c shows that the sorption isotherms can be indexed to type IV with an H1 hysteresis loop and a Brunauer-Emmett-Teller (BET) surface area of 339 m^2 g^{-1}; these results indicate the presence of mesopores in the structure. The H1 hysteresis loop indicates that the NSLCA has a clearly narrow pore size distribution, as illustrated in Fig. 3d. The pore size distribution of approximately 6.5 nm is observed using the Barrett-Joyner-Halenda (BJH) model for analysis. The narrow pore size distribution is likely linked to the porous MgO template.

In addition, X-ray photoelectron spectroscopy (XPS) technique was employed to investigate the chemical states and elemental ratios of N and S. The survey XPS spectrum of the NSLCA is shown in Fig. 3e. Only elements of C, O, N and S can be detected, and the atomic contents of N and S are 9.5% and 1.7%, respectively. The higher N content compared to the EDS results implies that the doped N is mostly adsorbed on the surface of the NSLCA sample. Fig. 3g shows the N 1s XPS spectrum of the

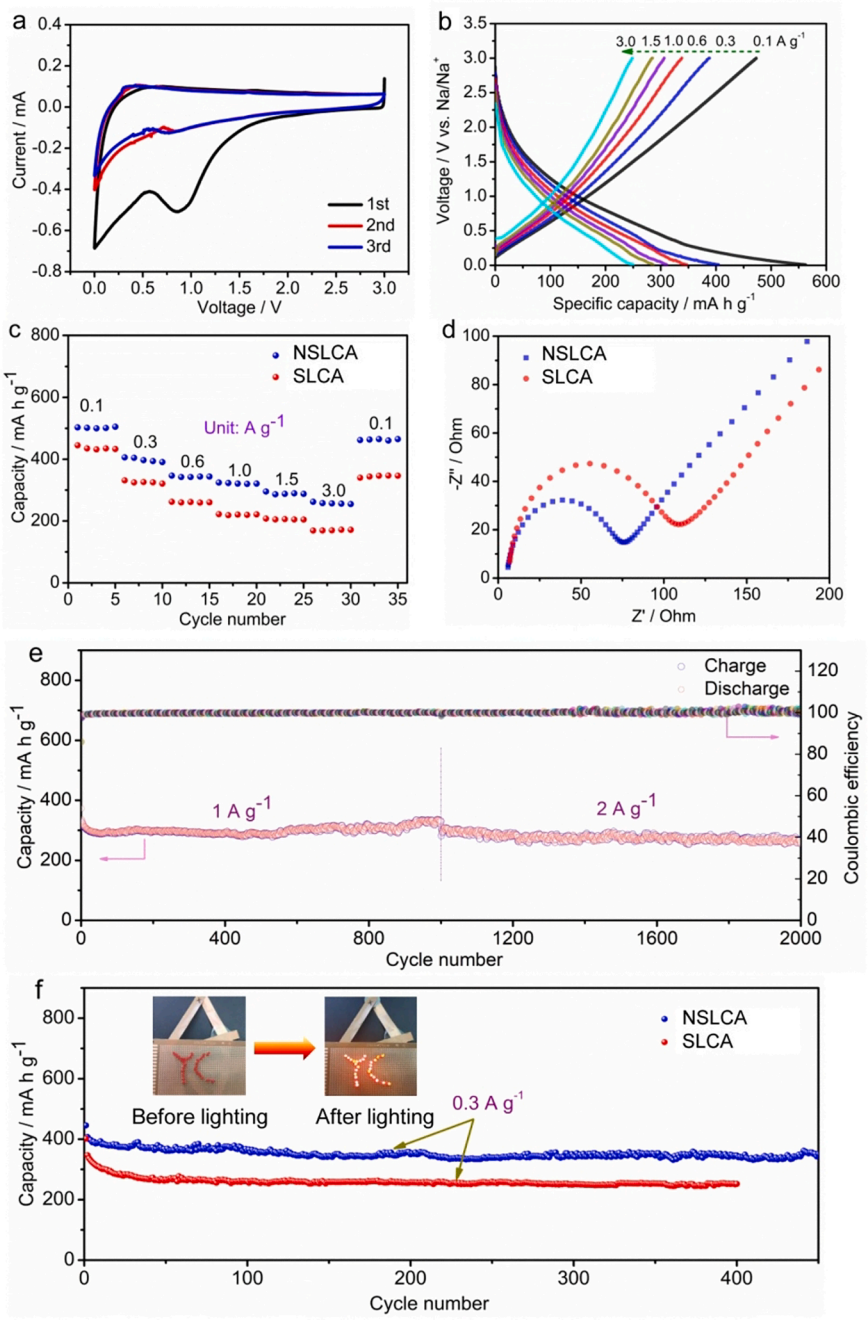

Fig. 4. (a) CV curves of the NSLCA from 3.0 to 0 V versus Na/Na^+ at a scan rate of 0.2 mV s^{-1}; (b) voltage profiles of the NSLCA electrodes at various current densities; (c) rate performance of the NSLCA electrodes; (d) Nyquist plots of the graphite and NSLCA; (e) cycling performance of the NSLCA electrodes at high current densities; and (f) cycling performance comparison of the NSLCA and SLCA electrodes at the same current density of 0.3 A g^{-1}. The inset shows the optical image of an LED panel powered by NSLCA anodic SIBs.

NSLCA nanosheets, and the peaks located at 398.6, 400 and 401 eV are attributed to pyridinic, pyrrolic and graphitic N, respectively [30]. The ratio of pyridinic, pyrrolic and graphitic N is estimated to be 1:0.74:0.84. It has been reported that pyridinic and pyrrolic N are chemically active and can reversibly bind with Na, strengthening the Na storage capability. Concurrently, graphitic N with three sp^2 carbon atoms plays an important role in improving the conductivity of graphitic carbon [31,32]. Therefore, in this work, the contents of different types of N can achieve a good balance while considering the capacity and rate performance of the NSLCA electrodes. Fig. 3h exhibits the S 2p XPS spectra of the NSLCA, and the peaks at 164 and 165.1 eV can be assigned to S $2p_{3/2}$ and $2p_{1/2}$, indicating that most of the S is integrated in the graphite matrix [33]. Additionally, the S 2p spectrum of the NSLCA contains a peak at 168.5 eV, which is attributed to oxidized S. The C 1s XPS spectrum of the NSLCA is shown in Fig. 3f. The deconvolution can be mainly divided into two peaks: a sharp peak at 284.7 eV (C–C bonds) and a broad peak at approximately 286 eV (C-O, C-N, etc.) [34]. In addition, Fourier transform infrared (FTIR) spectroscopy (Fig. 3i) also demonstrates the presence of S = O, C-N and C = N bonds.

To investigate the electrochemical behaviors of the synthesized NSLCA sample, a CR2025 coin-like half-cell was employed with a pure Na plate as a counter electrode to evaluate the electrochemical performance. The detailed cell assembly process is presented in the Experimental Section. The first three cycles of the cyclic voltammetry (CV) curves of the NSLCA electrode at a scan rate of 0.2 mV s^{-1} in the voltage range of 0.01 and 3.0 V (vs. Na/Na^+) are shown in Fig. 4a. In the first cathodic scan, the large broad peak occurring from 0.5 to 1.4 V and disappearing in the following cycles should be ascribed to the irreversible trapping of Na^+ into the samples and the generation of solid electrolyte interface (SEI) films on the surface of the electrode [24]. In

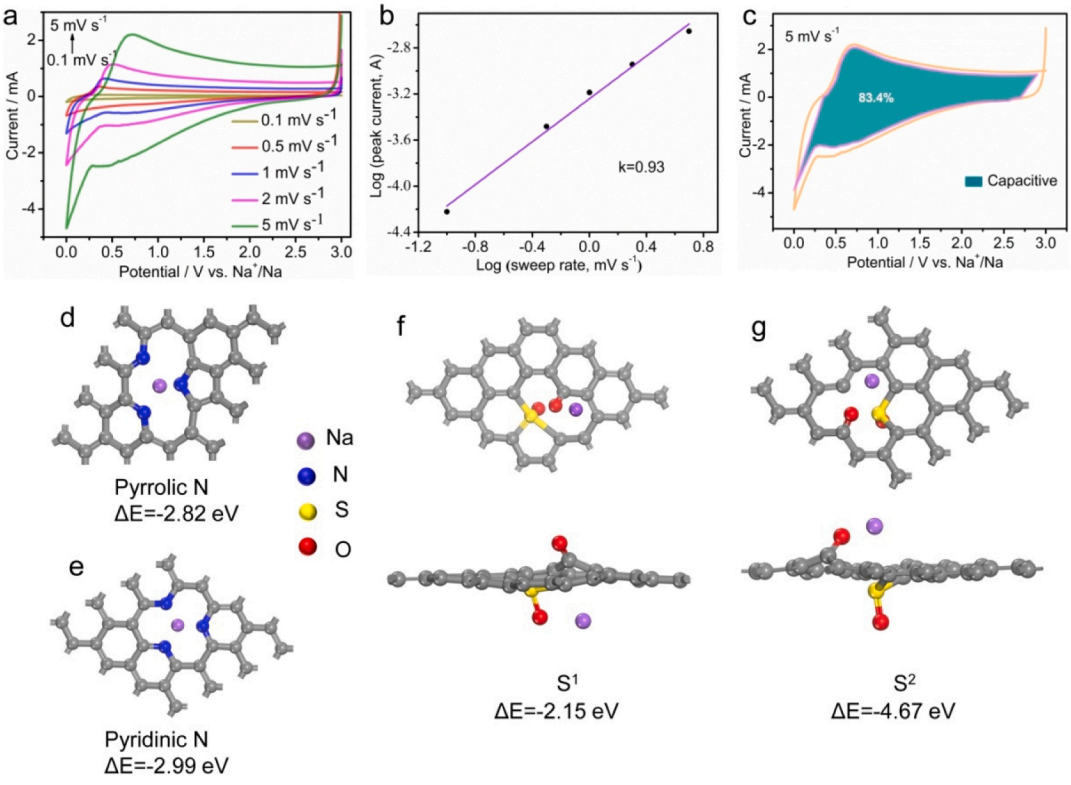

Fig. 5. The calculated sodium storage mode and kinetics analysis for NSLCA nanosheet electrodes: (a) CV curves at various scan rates[1]; (b) b-value derived from the relationship between the scan rates and peak currents; (c) separation of the capacitive (green region) and diffusion currents of the NSLCA nanosheet electrode at a scan rate of 5 mV s^{-1}. Optimized structure and adsorbability of the (d) pyrrolic N, (e) pyridinic N, and (f) and (g) S at different locations. (For interpretation of the references to colour in this figure legend, the reader is referred to the web version of this article.)

addition, it is observed that there are obvious anodic peaks at approximately 0.5 V, which is induced by the reversible intercalation and deintercalation reactions between Na^+ and the active sites in the samples.

Fig. 4b presents the first discharge–charge voltage profiles of the NSLCA electrode at different current densities. It is clearly shown that the trend in the discharge–charge voltage profiles remains almost unchanged even when the current density increases to 3 A g^{-1}, implying the excellent electrochemical performance of the NSLCA electrode. Furthermore, the rate performance of the NSLCA electrode is shown in Fig. 4c. Notably, the electrode was activated at a low current density for several cycles before testing. The NSLCA electrode delivers high specific capacities of 500, 404, 342, 321, 287, and 256 mA h g^{-1} at current densities of 0.1, 0.3, 0.6, 1, 1.5, and 3 A g^{-1}, respectively. Importantly, the NSLCA electrode exhibits good reversibility, with the specific discharge capacity recovering to the initial value while the current density returns to 0.1 A g^{-1}. For comparison, the SLCA electrode without doped N only delivers 430, 325, 260, 220, 204, and 170 mA h g^{-1} at the same current densities listed above. Hence, the doped N plays an important role in enhancing the rate performance of NSLCA electrodes. As shown in Fig. 4d, the NSLCA electrode exhibits a lower internal resistance than that of SLCA, indicating that doped graphitic N enables higher conductivity. The long-term cycling stability of the NSLCA and SLCA electrodes are shown in Fig. 4e and f. Notably, the NSLCA electrode displays superior stability even after deep charge and discharge cycles. The NSLCA electrode delivers high reversible specific discharge capacities of 290 and 270 mA h g^{-1} even after cycling at high current densities of 1 and 2 A g^{-1} 2000 cycles, respectively. For comparison, as illustrated in Fig. 4f, the NSLCA electrode delivers a stable ~400 mA h g^{-1} and the SLCA electrode shows a significantly decreased specific capacity of ~250 mA h g^{-1} at the same current density of 0.3 A g^{-1}. A light-emitting diode (LED) panel consisting of 27 LEDs with a pattern of a "YC" logo can be powered by NSLCA anodic LIBs after charging, as illustrated in the inset of Fig. 4f. The surface morphologies of the NSLCA electrode before and after cycling were characterized by SEM; the results are presented in Fig. S2. Fig. S2a and b shows the pristine NSLCA nanosheet electrode after charge–discharge for 500 cycles at a current density of 0.5 A g^{-1}. As shown in Fig. S2c and d, no obvious cracks or breakage can be found, indicating the excellent stability of the NSLCA electrode.

To uncover the electrochemical Na storage mechanism of the NSLCA electrodes, CV analysis at different scan rates was carried out. Fig. 5a shows the CV curves of the NSLCA electrode at various current densities between 0.1 and 5 mV s^{-1}. It possesses a pair of broad peaks with anodic and cathodic scanning due to Na trapping and extraction. A power-law model is utilized to qualitatively evaluate the capacitive effect, and the peak current (i) and scan rate (v) of the CV curves are important parameters for constructing the model ($i = av^b$)[35]. The slope of $log(i) - log(v)$ is defined as the b value. Generally, b values of 1.0 and 0.5 mean that the conversion reaction is based on capacitive effects and diffusion-controlled processes, respectively. As shown in Fig. 5b, the fitted b value of the NSLCA electrode is 0.93, shows significantly larger than 0.5 when the scan rate is lower than 5 mV s^{-1}. This result illuminates that the reversion reaction is kinetically controlled by the surface-induced capacitive effect. Fig. 5c shows that the capacitive reaction contributes 83.4% of the total capacity at 5 mV s^{-1}. The peak voltage is mainly ascribed to the diffusion-controlled charge, which principally lies in the doped N; notably, the high proportion of capacitance contribution is remarkably beneficial for improving the rate capability of the NSLCA electrodes.

In addition, to further understand the Na storage mechanism, first-principle calculations based on density functional theory (DFT) calculations were performed to determine the active sites for Na trapping. To elucidate the synergistic effects of S and N codoping, all reasonable

molecular models were optimized. As illustrated in Fig. 5d-g, the calculated binding energies of Na^+ on pyrrolic N, pyridinic N, and two different S sites are −2.82, −2.99, −2.15 and −4.67 eV, respectively. Hence, the DFT calculations show that both N and S doping can improve the Na storage capacity. Specifically, the capacity contributions from the N species are mainly from pyrrolic and pyridinic N. Moreover, the doped S can significantly increase the interlayer of graphite from 0.68 nm to 0.77 nm, as shown in Fig. S3, and the calculated value matches well with the TEM results.

4. Conclusions

In summary, a novel spongy-like N, S-codoped layered carbon assembly (NSLCA) was fabricated by a facile template method for sodium storage. Petroleum-derived pitch served as the carbon skeleton, and melamine and porous MgO acted as the nitrogen source and hard template, respectively. The NSLCA electrode possessed some unique advantages. First, the synthesis method made the utmost of the sulfur contained in the pitch, making it simple to realize mass production. Concurrently, the doped N content on the carbonaous surface was as high as 9.5%. Second, the doped N and S were both beneficial to improving the sodium storage capacity. Combined with theoretical calculations, pyrrolic and pyridinic N were the main N species contributing capacity. Third, the doped S significantly increased the interlayer of carbon, making it possible to intercalate more sodium atoms. Fourth, the unique assemblied conductive network artitectures also endows the NSLCA electrode excellent electrochemical performance in terms of both lifespan and rate capability; furthermore, this electrode delivered a high specific capacity of approximately 270 mA h g^{-1} even after cycling at high current densities of 1 and 2 A g^{-1} 2000 times. It is believed that this work will provide a simple and novel approach to produce dual component-doped carbonous materials on a large scale, effectively boosting the commercial application of sodium-ion batteries.

Declaration of Competing Interest

The authors declare that they have no known competing financial interests or personal relationships that could have appeared to influence the work reported in this paper.

Acknowledgments

The research was financially supported by the National Key Research and Development Program of China (2017YFA0208200), the Projects of NSFC (22022505, 21872069, 51761135104), the Fundamental Research Funds for the Central Universities of China (0205-14380219, 0205-14913212), the Natural Science Foundation of Jiangsu Province (BK20181056, BK20180008), Jiangsu Postdoctoral Science Fundation (2020Z258), the Natural Science Foundation of the Jiangsu Higher Education Institutions of China (20KJB530015) and the Shenzhen Fundamental Research Program of Science, Technology and Innovation Commission of Shenzhen Municipality (JCYJ20180307155007589).

Appendix A. Supplementary data

Supplementary data to this article can be found online at https://doi.org/10.1016/j.flatc.2021.100258.

References

[1] T. Liu, Y. Zhang, Z. Jiang, X. Zeng, J. Ji, Z. Li, X. Gao, M. Sun, Z. Lin, M. Ling, J. Zheng, C. Liang, Exploring competitive features of stationary sodium ion batteries for electrochemical energy storage, Energy Environ. Sci. 12 (2019) 1512–1533.
[2] M. Pasta, C.D. Wessells, N. Liu, J. Nelson, M.T. McDowell, R.A. Huggins, M. F. Toney, Y. Cui, Full open-framework batteries for stationary energy storage, Nat. Commun. 5 (2014) 3007.
[3] Y.E. Durmus, H. Zhang, F. Baakes, G. Desmaizieres, H. Hayun, L. Yang, M. Kolek, V. Küpers, J. Janek, D. Mandler, S. Passerini, Y. Ein-Eli, Side by Side Battery Technologies with Lithium-Ion Based Batteries, Adv. Energy Mater. 10 (2020) 2000089.
[4] M. Li, J. Lu, Z. Chen, K. Amine, 30 Years of Lithium-Ion Batteries, Adv. Mater. 30 (2018) 1800561.
[5] P.K. Nayak, L. Yang, W. Brehm, P. Adelhelm, From Lithium-Ion to Sodium-Ion Batteries: Advantages, From Lithium-Ion to Sodium-Ion Batteries: Advantages, Challenges, and Surprises, Angew. Chem. Int. Ed. 57 (2018) 102–120.
[6] L. Ma, J. Wu, G. Zhu, Y. Lv, Y. Zhang, H. Pang, Recent advances in two-dimensional materials for alkali metal anodes, J. Mater. Chem. A 9 (2021) 5232–5257.
[7] L. Ma, J. Cui, S. Yao, X. Liu, Y. Luo, X. Shen, J.-K. Kim, Dendrite-free lithium metal and sodium metal batteries, Energy Storage Mater. 27 (2020) 522–554.
[8] W. Ko, T. Park, H. Park, Y. Lee, K.E. Lee, J. Kim, $Na_{0.97}KFe(SO_4)_2$: an iron-based sulfate cathode material with outstanding cyclability and power capability for Na-ion batteries, J. Mater. Chem. A 6 (2018) 17095–17100.
[9] Y. Xu, X. Li, J. Wang, Q. Yu, X. Qian, L. Chen, Y. Dan, Fe-Doped CoP Flower-Like Microstructure on Carbon Membrane as Integrated Electrode with Enhanced Sodium Ion Storage, Chem. Eur. J. 26 (2020) 1298–1305.
[10] S. Alvin, H.S. Cahyadi, J. Hwang, W. Chang, S.K. Kwak, J. Kim, Revealing the Intercalation Mechanisms of Lithium, Sodium, and Potassium in Hard Carbon, Adv. Energy Mater. 10 (2020) 2000283.
[11] J.-Y. Hwang, H.-L. Du, B.-N. Yun, M.-G. Jeong, J.-S. Kim, H. Kim, H.-G. Jung, Y.-K. Sun, Carbon-Free TiO_2 Microspheres as Anode Materials for Sodium Ion Batteries, ACS Energy Lett. 4 (2019) 494–501.
[12] G. Cha, S. Mohajernia, N.T. Nguyen, A. Mazare, N. Denisov, I. Hwang, P. Schmuki, Li^+ Pre-Insertion Leads to Formation of Solid Electrolyte Interface on TiO_2 Nanotubes That Enables High-Performance Anodes for Sodium Ion Batteries, Adv. Energy Mater. 10 (2020) 1903448.
[13] L. Cheng, Y. Zhang, P. Chu, S. Wang, Y. Li, X. Ren, P. Zhang, L. Sun, Heterostructure enhanced sodium storage performance for SnS_2 in hierarchical SnS_2/Co_3S_4 nanosheet array composite, J. Mater. Chem. A 9 (2021) 1630–1642.
[14] Y. Jiang, D. Song, J. Wu, Z. Wang, S. Huang, Y. Xu, Z. Chen, B. Zhao, J. Zhang, Sandwich-like SnS_2/Graphene/SnS_2 with Expanded Interlayer Distance as High-Rate Lithium/Sodium-Ion Battery Anode Materials, ACS Nano 13 (2019) 9100–9111.
[15] J. Ru, T. He, B. Chen, Y. Feng, L. Zu, Z. Wang, Q. Zhang, T. Hao, R. Meng, R. Che, C. Zhang, J. Yang, Covalent Assembly of MoS_2 Nanosheets with SnS Nanodots as Linkages for Lithium/Sodium-Ion Batteries, Angew. Chem. Int. Ed. 59 (2020) 14621–14627.
[16] K. Ma, Y. Dong, H. Jiang, Y. Hu, P. Saha, C. Li, Densified MoS_2/Ti_3C_2 films with balanced porosity for ultrahigh volumetric capacity sodium-ion battery, Chem. Eng. J. 127479 (2020).
[17] J. Huang, X. Guo, X. Du, X. Lin, J.-Q. Huang, H. Tan, Y. Zhu, B. Zhang, Nanostructures of solid electrolyte interphases and their consequences for microsized Sn anodes in sodium ion batteries, Energy Environ. Sci. 12 (2019) 1550–1557.
[18] W. Brehm, J.R. Buchheim, P. Adelhelm, Reactive and Nonreactive Ball Milling of Tin-Antimony (Sn-Sb) Composites and Their Use as Electrodes for Sodium-Ion Batteries with Glyme Electrolyte, Energy Technol. 7 (2019) 1900389.
[19] S. Zhu, Q. Li, Q. Wei, R. Sun, X. Liu, Q. An, L. Mai, $NiSe_2$ Nanooctahedra as an Anode Material for High-Rate and Long-Life Sodium-Ion Battery, ACS Appl. Mater. Interfaces 9 (2017) 311–316.
[20] H. Hou, C.E. Banks, M. Jing, Y. Zhang, X. Ji, Carbon Quantum Dots and Their Derivative 3D Porous Carbon Frameworks for Sodium-Ion Batteries with Ultralong Cycle Life, Adv. Mater. 27 (2015) 7861–7866.
[21] G. Yang, X. Li, Z. Guan, Y. Tong, B. Xu, X. Wang, Z. Wang, L. Chen, Insights into Lithium and Sodium Storage in Porous Carbon, Nano Lett. 20 (2020) 3836–3843.
[22] X. Sun, C. Wang, Y. Gong, L. Gu, Q. Chen, Y. Yu, A Flexible Sulfur-Enriched Nitrogen Doped Multichannel Hollow Carbon Nanofibers Film for High Performance Sodium Storage, Small 14 (2018) 1802218.
[23] J. Ye, J. Zang, Z. Tian, M. Zheng, Q. Dong, Sulfur and nitrogen co-doped hollow carbon spheres for sodium-ion batteries with superior cyclic and rate performance, J. Mater. Chem. A 4 (2016) 13223–13227.
[24] H. Wang, H. Yuan, W. Zhan, Y.-S. Lee, H.-J. Shin, X. Wei, Q. Cai, J.-L. Lan, Y. Yu, X. Yang, Integrated N, P co-doped and dense carbon networks produced by a chemical crosslinking strategy: Facilitating high gravimetric/volumetric performance sodium ion batteries, Carbon 165 (2020) 204–215.
[25] P.E. Blöchl, Projector augmented-wave method, Physical Review B 50 (1994) 17953–17979.
[26] J.P. Perdew, K. Burke, M. Ernzerhof, Generalized Gradient Approximation Made Simple, Physical Review Letters 77 (1996) 3865–3868.
[27] P.-J. Wang, D. Zhou, H.-H. Guo, W.-F. Liu, J.-Z. Su, M.-S. Fu, C. Singh, S. Trukhanov, A. Trukhanov, Ultrahigh enhancement rate of the energy density of flexible polymer nanocomposites using core–shell $BaTiO_3$@MgO structures as the filler, J. Mater. Chem. A 8 (2020) 11124–11132.
[28] Y. Zhao, Z. Liu, W. Chu, L. Song, Z. Zhang, D. Yu, Y. Tian, S. Xie, L. Sun, Large-Scale Synthesis of Nitrogen-Rich Carbon Nitride Microfibers by Using Graphitic Carbon Nitride as Precursor, Adv. Mater. 20 (2008) 1777–1781.
[29] D. Kesavan, V.K. Mariappan, K. Krishnamoorthy, S.-J. Kim, Carbothermal conversion of boric acid into boron-oxy-carbide nanostructures for high-power supercapacitors, J. Mater. Chem. A 9 (2021) 915–921.
[30] Y. Zhou, L. Zhang, W. Huang, Q. Kong, X. Fan, M. Wang, J. Shi, N-doped graphitic carbon-incorporated g-C_3N_4 for remarkably enhanced photocatalytic H_2 evolution under visible light, Carbon 99 (2016) 111–117.

[31] W. Lei, W. Xiao, J. Li, G. Li, Z. Wu, C. Xuan, D. Luo, Y.-P. Deng, D. Wang, Z. Chen, Highly Nitrogen-Doped Three-Dimensional Carbon Fibers Network with Superior Sodium Storage Capacity, ACS Appl. Mater. Interfaces 9 (2017) 28604–28611.
[32] Y.-E. Zhu, L. Yang, X. Zhou, F. Li, J. Wei, Z. Zhou, Boosting the rate capability of hard carbon with an ether-based electrolyte for sodium ion batteries, J. Mater. Chem. A 5 (2017) 9528–9532.
[33] M. Klingele, C. Pham, K.R. Vuyyuru, B. Britton, S. Holdcroft, A. Fischer, S. Thiele, Sulfur doped reduced graphene oxide as metal-free catalyst for the oxygen reduction reaction in anion and proton exchange fuel cells, Electrochem. Commun. 77 (2017) 71–75.
[34] X. Wang, J. Wang, D. Wang, S. Dou, Z. Ma, J. Wu, L. Tao, A. Shen, C. Ouyang, Q. Liu, S. Wang, One-pot synthesis of nitrogen and sulfur co-doped graphene as efficient metal-free electrocatalysts for the oxygen reduction reaction, Chem. Commun. 50 (2014) 4839–4842.
[35] A. Haffner, A.-K. Hatz, I. Moudrakovski, B.V. Lotsch, D. Johrendt, Fast Sodium-Ion Conductivity in Supertetrahedral Phosphidosilicates, Angew. Chem. Int. Ed. 57 (2018) 6155–6160.